SCIENCE CHINA
Information Sciences

• RESEARCH PAPER •

October 2018, Vol. 61 102301:1–102301:8
https://doi.org/10.1007/s11432-017-9277-x

Multi-scale rock detection on Mars

Guoqing LI[1], Yunhai GENG[1] & Xueming XIAO[1,2*]

[1] *School of Astronautics, Harbin Institute of Technology, Harbin* 150001*, China;*
[2] *School of Opto-Electronic Engineering, Changchun University of Science and Technology, Changchun* 130022*, China*

Received 31 May 2017/Revised 13 August 2017/Accepted 10 October 2017/Published online 18 May 2018

Abstract In this paper, we propose a novel autonomous Martian rock detection framework via superpixel segmentation. Different from current state-of-the-art pixel-level rock segmenting methods, the proposed method deals with this issue in region level. Image is splitted into homogeneous regions based on intensity information and spatial layout. The heart of proposed framework is to enhance such region contrast. Then, rocks can be simply segmented from the resulting contrast-map by an adaptive threshold. Our method is efficient in dealing with large image and only few parameters need to set. Preliminary experimental results show that our algorithm outperforms edge-based methods in various grayscale rover images.

Keywords Mars rover, rock detection, superpixel segmentation, region contrast, image enhancement

Citation Li G Q, Geng Y H, Xiao X M. Multi-scale rock detection on Mars. Sci China Inf Sci, 2018, 61(10): 102301, https://doi.org/10.1007/s11432-017-9277-x

1 Introduction

Rock detection and recognition on Mars is the basis of hazard avoidance and path planning in Mars rover missions. Using the grayscale images captured by the panoramic cameras, rocks can be detected by auto rock detection algorithms. Current state-of-the-art image segmentation algorithms [1–3] usually use the edge-based techniques to identify closed rock contours.

One of the most significant problems of such boundary-based detectors is the poor precision of rock detection. It is difficult to extract rocks boundaries from intensity images. Different from relatively regular craters, rocks exhibit diverse morphologies, textures or other properties against soil of Mars [4, 5]. Such diversities are the leading cause of poor precision for edge-based visual segmentation techniques. Meanwhile, impacts of complex illumination conditions and dust covering leads to shadows and boundary blurring, which accentuated the predicament of rock detection techniques [6]. As a result, rock detection still remains an interesting yet challenging topic in the past few decades.

The fundamental technique of edge extraction methods basically is local intensity-gradient operator. Rock boundaries are firstly detected by gradient operator, after that edge-linking and gap filling procedures are used to group boundaries into contours. Such methods are well-performed detecting "dry" rocks with totally closed and obvious contours. However, one of the major obstacles of local intensity-gradient is the sensitivity to noise, which seriously affect the identification of rocks with dusty or blur boundaries. Figure 1 shows some typical scenes that edge-based methods failed to segment evident rocks (red rectangle) or occurred large portion of false (blue rectangle).

Several attempts have been made to solve this issue. Instead of extracting boundaries, some of them utilized shadows to find rocks, such as the Marsokhod shadow detector [7]. Refs. [8, 9] modeled rocks by

* Corresponding author (email: alexcapshow@gmail.com)

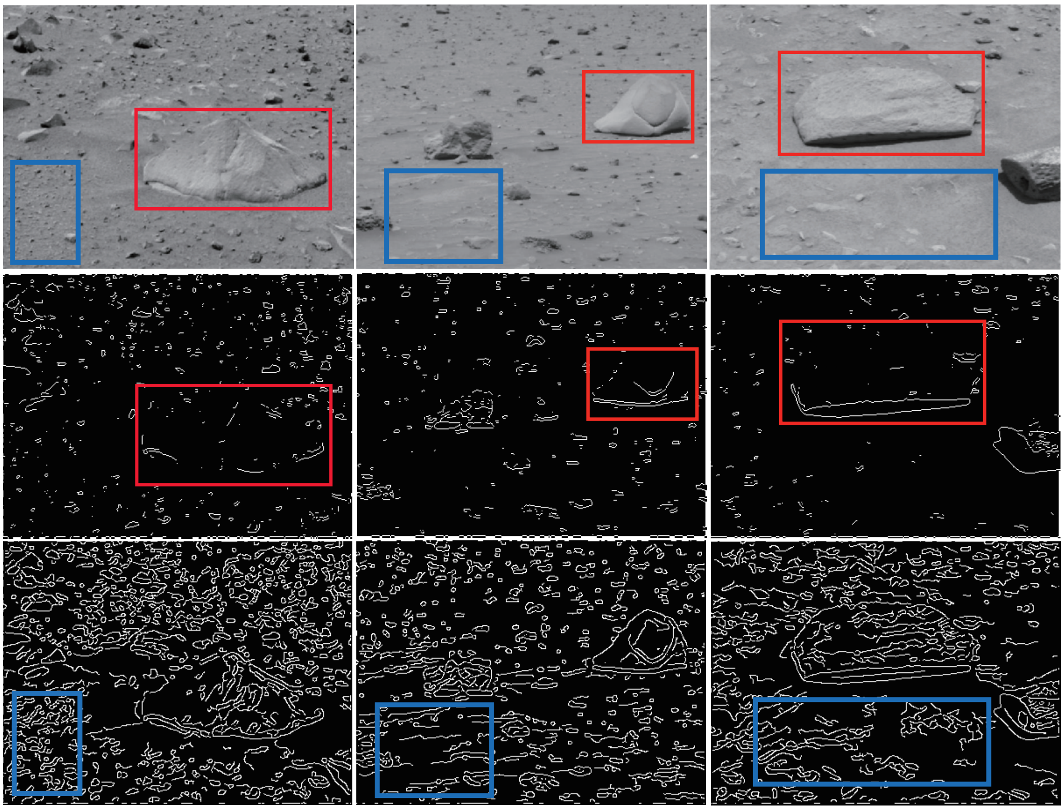

Figure 1 (Color online) Some of the notable rocks on Mars that edge detection algorithms failed to attach contours or generated false boundaries. From top to bottom: grayscale images taken by Spirit Rover's pancam; edge maps obtained by Sobel detector; results from Canny operator.

shadows for spacecraft safe landing missions. However, shadow-based detectors lack accurate boundary attachment since they apply ellipse profile to roughly cover the rocks. Some studies [10,11] suggest that the stereo-based approaches may play an alternative way to resolve this problem by providing depth information which passive image lacked. Similar with this, 3D Lidar-based methods are also recorded in recent work [12,13]. Moreover, there are efforts using supervised learning strategy [5,14], which explored the redundant features associated with rocks. By manually marking the rocks, rock features are learned by support vector machine (SVM) classifier or other classification algorithms, the resulting features are applied to detect rocks. A key issue of supervised learning is the lack of a sufficient rock database. It is impossible to obtain all the diverse rocks on Mars environment.

Because the visual detection literatures on object detection and segmentation are vast, in above discussion, we only focus on some typical papers for onboard application. Current state-of-the-art visual detection or segmentation methods may also show some possibilities for onboard application with the hardware improvement of onboard computer. Recently, self-paced learning methodologies [15,16] show significant potential to deal with complex detection issues. One of the major challenges is the variety and complexity of practical images, it is very hard to well annotated such samples for training set establishment. Self-paced learning can effectively solve this issue by pseudo-labeling the images and then feeding them back into training. There is a detail about current development or application of self-paced learning on the web-page[1)] by Meng, who did a pioneer study on this topic.

Results from above studies demonstrate a strong and consistent association between detection precision and the application of multi-sensors or multi-features. Since edge-based framework does not fully utilize spatial layout and intensity relationship of pixels or regions, such multi-scale strategy may be better for revealing inner difference between background and foreground.

In this paper, we propose a multi-scale rock detection method solely based on low-level features. Image

1) http://gr.xjtu.edu.cn/web/dymeng/6.

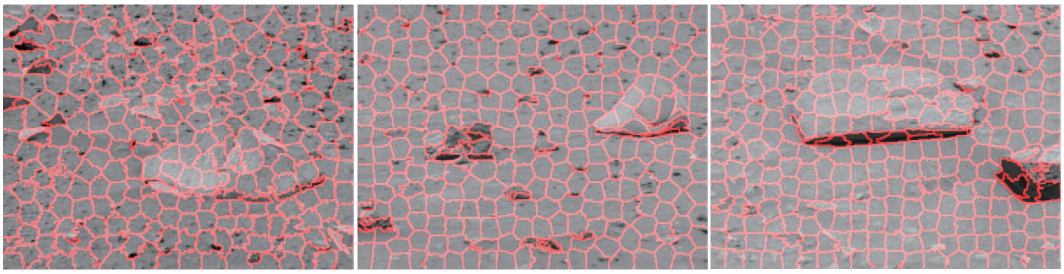

Figure 2 (Color online) Superpixel of Mars images.

is grouped into perceptually meaningful atomic regions in multi-scale, on each scale, mean intensity and standard variation of each region are measured. We deal with the rock detection as a result of contrast enhancement, which is derived as the intensity difference of any pair of superpixels and weighted by the integration of spatial location constraint and a smooth term. It is based on the fact that generally rocks have higher reflectivity than background soil under strong Martian illumination environment. As a result, the front side of rocks will get higher intensity values than the soil, while achieve lower pixel values at their shading areas. Therefore, region contrast can be denoted as the measurement of possibility that a specific superpixel belonging to rock or soil. To generate contrast map, resulting region contrast on each scale is further normalized to $[0,1]$. Rock regions will take large values close to 1, while background is near 0 in resulting contrast map. Multi-scale superpixel segmentation is used to produce varying-scale local contrast information, since fixed superpixel number strategy may face the dilemmas between the over-segmentation and the under-segmentation. Contrast maps on each scale were calculated and then fused together to produce the final map. Threshold the map using an adaptive threshold to obtain the detection results.

The remainder of the paper is constructed as follows: in Section 2, we introduce the proposed method; Section 3 shows the results and evaluates the performance using real Mars images; Section 4 concludes the paper.

2 Methodology

2.1 Region generation

Image is firstly splitted into homogeneous subregions by intensity and spatial layout at a specific segmentation scale k. N^k denotes the number of superpixels N at k. We utilize simple linear iterative clustering (SLIC) method [17] to generate superpixels for its almost linear complexity $\mathcal{O}(N)$ and fine boundaries adherence. The distance between two subregions is measured as

$$D = \sqrt{d_I^2 + \left(\frac{d_s}{S}\right)^2 (m^k)^2}, \tag{1}$$

where d_I denotes the intensity difference and d_s measures the Euclidean distance, m^k balances the weight between intensity similarity and spatial proximity at scale k. Large m^k demonstrates the spatial proximity, and vice versa. d_I and d_s are defined as following formulas, respectively:

$$d_I = |I_i - I_j|, \tag{2}$$

$$d_s = \sqrt{(x_i - x_j)^2 + (y_i - y_j)^2}. \tag{3}$$

Figure 2 presents resulting superpixels of image in Figure 1 at different segmentation scales.

2.2 Superpixel contrast

After splitting, image I was transformed into a subregion set $\boldsymbol{\mathcal{S}} = \{S \mid S_i, i = 1, 2, \ldots, N\}$. Statistical features involving mean intensity In_i and texture detector Sm_i are used to measure the characteristic of each S_i.

$$\text{In}_i = \text{mean}(S_i), \tag{4}$$

$$\text{Sm}_i = 1 - \frac{1}{1+\sigma(S_i)}, \tag{5}$$

where $\sigma(S_i)$ denotes the variation of S_i. Sm_i is normalized to $[0, 1]$. For subregions belong to flat background, Sm_i is close to 0, while rocks with rich texture surface will achieve value near 1.

Spatial constraint is also taken into account, since the size of any rock in an image is limited. In order to emphasize the locality of rock sizes, we define the spatial location factor of rock w_d as follows:

$$w_d = \exp\left(-\frac{d_s}{\sigma_s}\right), \tag{6}$$

where d_s denotes the Euclidean distance of each pair of superpixels' center (x_i^c, y_i^c):

$$d_s = \sqrt{(x_i^c - x_j^c)^2 + (y_i^c - y_j^c)^2}. \tag{7}$$

Superpixel contrast R is then derived as the integration of intensity difference and spatial factor, as well as the texture descriptor

$$R(S_i) = \sum_{j=1}^{N} |\text{In}_i - \text{In}_j|\text{Sm}_i w_d. \tag{8}$$

2.3 Multi-scale fusion

In our latest study [18], we measure the contrast in fixed superpixel number and perform a favorable detection result. However, such onefold superpixel segmentation may lead to false adherence at blurring boundaries, which in turn results in detection errors involving the false detection and the missed detection. Although over-segmentation can provide detailed contrast information for small regions, it fails to measure the global or large-scale region contrast. On the contrary, under-segmentation gets the benefit of depicting large-scale contrast, but suffers the missing of detailed difference. It is difficult to solve the contradiction between the over-segmentation and under-segmentation by a regular scale. To handle this problem, superpixels at k scales are applied in this paper. Region contrast is computed on each scale and the final contrast map C is then fused by integrating such multi-scale results. Multi-scale segmentation can realize the complementary advantage by measuring the varying-scale local contrast. We denote the optimized multi-scale algorithm as RC*, and the initial specific scale version by RC.

$$C = \text{norm}\left(\sum_{i=1}^{k} R^k\right). \tag{9}$$

The final segmented rock image is obtained by cutting C map using an adaptive threshold T, in this paper, we define T as

$$T = \tau \times \text{ave}(C), \tag{10}$$

where $\tau = 2$ in our following experiments. Denote the binarized images as $(*)$ cut.

3 Experimental result

To validate the efficiency of proposed algorithms, experiments detailed in this section involved images drawn form both Spirit and Opportunity Mars rover pancams. Multi-scale superpixels parameters are listed in Table 1.

Unfortunately, there is no automatic scheme to determine both the number of scales and the corresponding parameters for each scale. We manually set the total numbers of segmentation scales and corresponding parameters N^i and m^i based on the sizes of obtained images. Since the sizes of images

Table 1 Parameters setting for multi-scale superpixels segmentation

Scale	1	2	3	4	5	6	7	8	9	10	11	12
N^i	250	300	350	400	450	500	550	600	650	700	750	800
m^i	5.5	5.5	7	7	8.5	8.5	10	10	11.5	11.5	13	13

captured by pancams are under 1k×1k, the largest superpixel number should be smaller than 1000, otherwise there will be no difference between proposed region-level method and current pixel-based algorithms. We set the max-segmentation number to be 800. The numbers of rest scales are decreasing progressively by 50 from initial 800 to the minimum number. In this paper, we set the min-segmentation number is 250.

As we mentioned in Subsection 2.1, m balances the weight between intensity difference and spatial proximity. Large m will result in relatively regular and compact superpixels. With small m, the resulting superpixels adhere more tightly to boundaries, yet have less regular size and shape [17]. In order to obtain efficient and reliable statistical features, there should have sufficient pixel numbers in each superpixel. In addition, the setting of m should guarantee each superpixel has approximate pixel numbers to reduce the influence of superpixel size, especially when the segmentation scale is large. Based on that, we set larger m in large-sale superpixel segmentation and smaller m for small-scale segmentation. In this paper, we set the maximum of m is 13, while the minimum is 5.5 (the recommendatory interval of m is $[1, 40]$ [17]). The rest is decreasing progressively by 1.5 until the minimum m has been reached.

In order to quantitatively evaluate the performance of proposed algorithms, both precision-recall cure (PRC) and area under receiver operating characteristics curve (AUC) are taken into consideration. We generate the segmentation results of contrast map at different thresholds ranging from 0 to 255 and compute the statistic metrics. AUC measures the probability that positive detection is ranked higher than negative example. High AUC value means the algorithm achieves convincing rock segmentation results. Precision is the percentage of true rocks to all the detected rocks, while the recall is the percentage of rocks segmented from the total rocks actually present in the scene. High PRC means algorithms returned substantially more relevant results than false ones. In addition, F_β (Fmea) is also used to combine precision and recall [18]:

$$F_\beta = \frac{(1+\beta^2)\text{Precision} \times \text{Recall}}{\beta^2 \times \text{Preciison} + \text{Recall}}. \tag{11}$$

Set $\beta^2 = 0.3$ to emphasize the precision than recall. Considering the difficulty of manually labeling rocks in the real Martian images, only 21 images were used to verify the statistic performance.

Figure 3 presents the statistical results. As can be seen, both RC and its optimization RC* achieves favorable results in PRC and AUC metrics. Maximum F_β for each algorithm is larger than 0.7. F_β of RC* is better than RC, indicates the efficiency of proposed multi-scale fusion. There is a clear fact that RC* does better than RC in PRC with any recall value, further manifesting the importance of taking multi-scale strategy in a computationally feasible framework. Taking 40% recall as a illustration, 83.1% in the precision of RC* was recorded, yet no statistically high precision of RC method was observed which was less than 80%. Any of the two methods reaches high AUC value larger than 0.7. RC* ranks the top with AUC 0.8072, F_β 0.7609.

Figure 4 shows some segmentation results of panoramic images by proposed methods. It is apparent that the detecting maps resulting from Canny operator does not achieve considerable performance as good as region-based methods. The differences between RC and RC* are evident and indicate the efficiency of multi-scale fusion as shown in the bottom of Figure 4. Meanwhile, the segmented comparisons between Figure 4(c) and (e) show that proposed method can significantly reduce the false detection. In summary, our method are well-performed in dealing with real Mars images.

To analysis the sensitivity of detection results to the above parameters, we carried more experiments by changing the segmentation scale k and m. First, the influence of m is tested by calculating statistical metrics under full scales ($k = 1, \ldots, 12$) with fixed $m = 5.5$ and 13, respectively. And then, only half of the total scales, under m shown in Table 1, is used to evaluate the effect of scale changing to the final detection results. To such, we firstly set half scales $k_1 = 1, \ldots, 6$, ant then $k_2 = 7, \ldots, 12$.

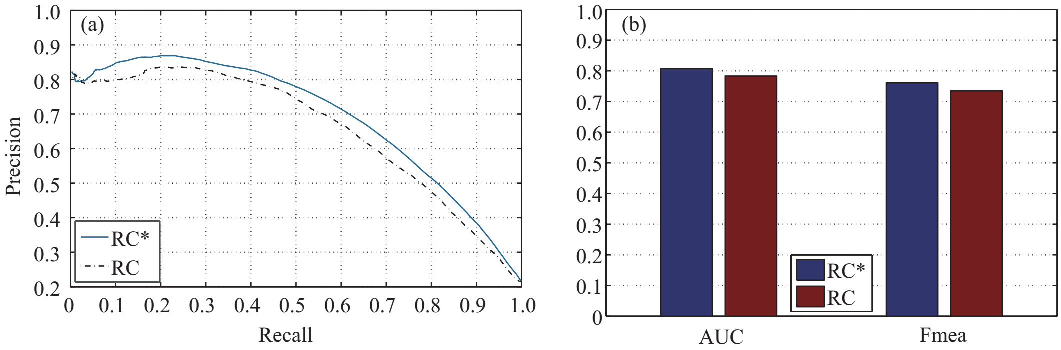

Figure 3 (Color online) Statistical performance on RC* and RC, respectively. (a) PRC curves; (b) AUC and Max-F_β.

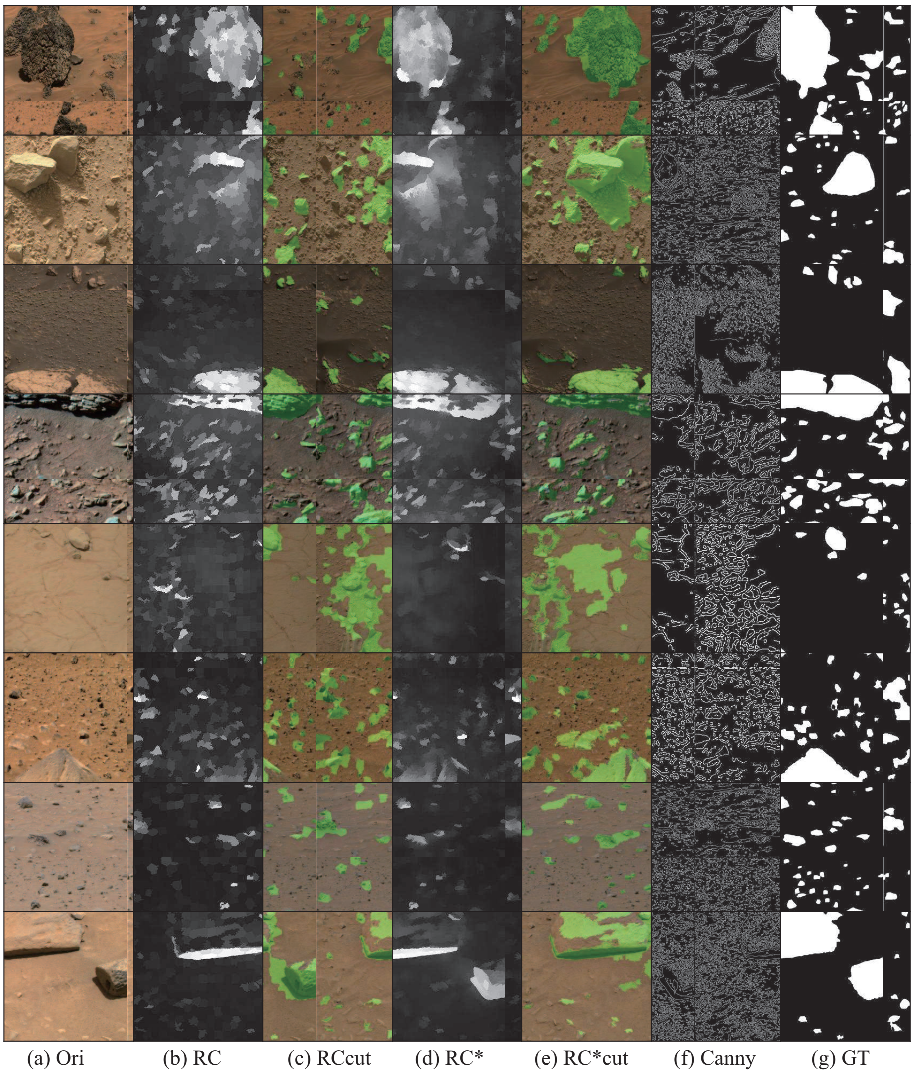

Figure 4 (Color online) Visual performance of proposed algorithm on real Martian images. (a) Original image; (b) and (d) are contrast maps resulting from RC and RC*, respectively; (c) and (e) are corresponding cutting maps; (f) the detecting results by Canny operator; (g) ground truth.

Figure 5 presents the statistical results compared with RC* and RC. As can be seen in resulting PRC profiles (Figure 5(a)), despite there exist slight differences between all of the above tests, they achieve consistent results with RC* (Figure 5(b)). Test with large m ($m = 13$) achieves higher PRC values than that under small one, which gets the maximum F_β 0.7615, slightly better than small one's 0.7472. For

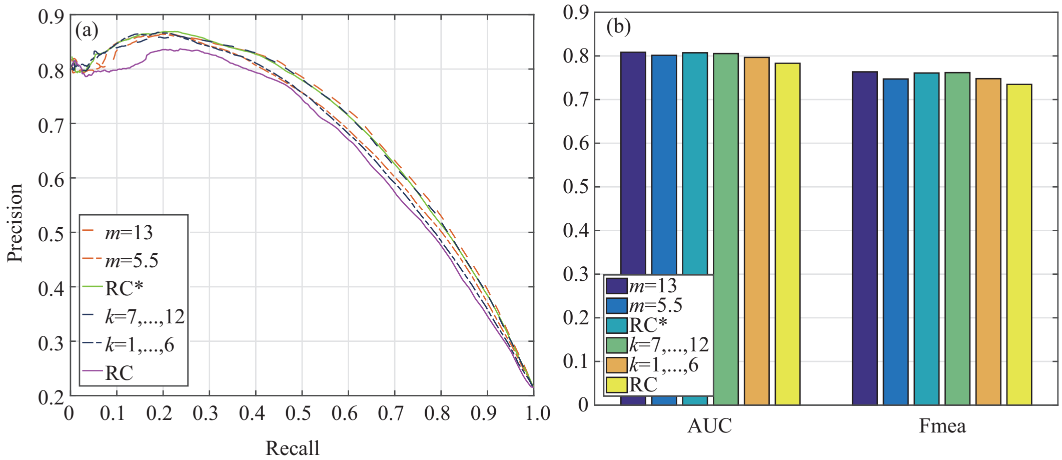

Figure 5 (Color online) Statistical performance on tests with parameters changing. (a) PRC curves; (b) AUC and Max-F_β.

RC*, the corresponding F_β value is 0.7609. On the evaluation of AUC, both of them are on par with RC*, achieving AUC of 0.8074 and 0.8015, respectively, while AUC of RC* is 0.8072. Similarly, tests with k changing is also taken into consideration. Statistical results under k_1 and k_2 are given in Figure 5. There is a clear fact that results under k_2 are better than those in k_1, which demonstrates the key role of large segmentation scales in multi-scale fusion algorithm like RC*. Test under k_2 achieves on-par performance with RC*, the corresponding AUC, F_β values are 0.8053 and 0.7617, respectively. Test under k_1 is not well-performed as RC* does. It gets the F_β of 0.7478 and the AUC value of 0.8015, both of the two statistical metrics are smaller than those of RC*. Nevertheless, it still gets better detection rate than RC. In fact, all the above statistical results are better than RC, demonstrating the superiority of multi-scale fusion strategy.

Such consistent performance directly indicate the insensitivity of detection results to parameters' changing. However, as we mentioned above, it will get better detection results under large segmentation scale and weight factor m. Therefore, the principle of parameter setting for proposed algorithm is to enlarge such scale and m, under allowed computational environment.

4 Conclusion and discussion

In this paper, we propose a novel rock detection method via multi-scale region contrast. Instead of detecting rock boundaries, new method deals with the detection processing as foreground enhancement. Only low-level features, mean intensity, standard variation and spatial constraint are utilized to model superpixel contrast. Proposed method achieves consistent and favorable results through real Mars images, demonstrating its efficiency in future Mars rover missions.

Acknowledgements This work was supported by National Natural Science Foundation of China (NSFC) (Grant Nos. 61503102, 61701225).

References

1 Castano R, Judd M, Estlin T, et al. Current results from a rover science data analysis system. In: Proceedings of IEEE Aerospace Conference, Big Sky, 2005
2 Thompson D R, Castano R. Performance comparison of rock detection algorithms for autonomous planetary geology. In: Proceedings of IEEE Aerospace Conference, Big Sky, 2007
3 Burl M C, Thompson D R, deGranville C, et al. Rockster: onboard rock segmentation through edge regrouping. J Aerosp Inf Syst, 2016, 13: 329–342
4 Spencer D A, Adams D S, Bonfiglio E, et al. Phoenix landing site hazard assessment and selection. J Spacecr Rocket, 2009, 46: 1196–1201

5 Dunlop H, Thompson D R, Wettergreen D. Multi-scale features for detection and segmentation of rocks in mars images. In: Proceedings of IEEE Conference on Computer Vision and Pattern Recognition, Minneapolis, 2007
6 Bonfiglio E P, Adams D, Craig L, et al. Landing-site dispersion analysis and statistical assessment for the Mars Phoenix lander. J Spacecr Rocket, 2011, 48: 784–797
7 Gulick V C, Morris R L, Ruzon M A, et al. Autonomous image analyses during the 1999 Marsokhod rover field test. J Geophys Res Planet, 2001, 106: 7745–7763
8 Huertas A, Cheng Y, Madison R. Passive imaging based multi-cue hazard detection for spacecraft safe landing. In: Proceedings of IEEE Aerospace Conference, Big Sky, 2006
9 Matthies L, Huertas A, Cheng Y, et al. Landing hazard detection with stereo vision and shadow analysis. In: Proceedings of IEEE International Conference on Robotics and Automation, Pasadena, 2007
10 Gor V, Mjolsness E, Manduchi R, et al. Autonomous rock detection for Mars terrain. In: Proceedings of AIAA Space Conference and Exposition, Albuquerque, 2001
11 Fox J, Castano R, Anderson R C. Onboard autonomous rock shape analysis for Mars rovers. In: Proceedings of IEEE Aerospace Conference, Big Sky, 2002
12 Di K C, Yue Z Y, Liu Z Q, et al. Automated rock detection and shape analysis from Mars rover imagery and 3D point cloud data. J Earth Sci, 2013, 24: 125–135
13 Xiao X M, Cui H T, Tian Y. Robust plane fitting algorithm for landing hazard detection. IEEE Trans Aerosp Electron Syst, 2015, 51: 2864–2875
14 Gong X J, Liu J L. Rock detection via superpixel graph cuts. In: Proceedings of the 19th IEEE International Conference on Image Processing, Orlando, 2012. 2149–2152
15 Ma F, Meng D Y, Xie Q, et al. Self-paced co-training. In: Proceedings of International Conference on Machine Learning, Sydney, 2017. 2275–2284
16 Zhang D W, Meng D Y, Han J W. Co-Saliency detection via a self-paced multiple-instance learning framework. IEEE Trans Pattern Anal Mach Intel, 2017, 39: 865–878
17 Achanta R, Shaji A, Smith K, et al. SLIC superpixels compared to state-of-the-art superpixel methods. IEEE Trans Pattern Anal Mach Intel, 2012, 34: 2274–2282
18 Xiao X M, Cui H T, Yao M B, et al. Autonomous rock detection on Mars through region contrast. Adv Space Res, 2017, 60: 626–635